

光学学报

基于光敏硅的多功能可重构超表面

任佳慧, 李九生*

中国计量大学太赫兹研究所, 浙江 杭州 310018

摘要 提出一种双 C 环光敏硅可重构超表面, 该超表面通过改变光敏硅电导率可以实现在太赫兹波段的多功能切换。当大小 C 环的电导率分别为 5.0×10^5 S/m 和 0 S/m 时, 所设计超表面表现为线-线极化转换器, 在 2.10~3.15 THz 频率范围内极化转换率大于 90%; 当大小 C 环的电导率分别为 0 S/m 和 5.0×10^5 S/m, 该结构在 2.33~2.47 THz 和 2.78~4.40 THz 频率范围内表现为线-圆极化转换器; 当大小 C 环的电导率同时变化为 2.5×10^5 S/m 时, 该结构转化为吸收器, 在 2.40~4.60 THz 频率范围内吸收率大于 90%。将大小 C 环电导率都为 0 S/m 的单元与大小环电导率都为 2.5×10^5 S/m 的单元进行编码, 该结构在 2.80~3.00 THz 范围内实现近场成像。将大小 C 环电导率分别为 5.0×10^5 S/m 和 0 S/m 的单元与大小环电导率都为 0 S/m 的单元进行周期性编码, 该结构可实现对太赫兹波二分束和四分束。结果表明, 通过改变外部光照条件, 可以实现对所设计超表面重构, 获得多种太赫兹调控功能。

关键词 表面光学; 太赫兹; 光敏硅; 可重构超表面; 多功能

中图分类号 O436 **文献标志码** A

DOI: 10.3788/AOS222075

1 引言

超表面是一种人工复合二维表面, 具有结构简单、易于制造、便于集成的特性, 同时具备较强的相位控制能力^[1-3], 在太赫兹滤波器^[4-5]、吸收器^[6-7]、偏振转换器^[8-9]、调制器^[10]制备, 以及波前调控^[11-12]和成像^[13-14]等方面具有良好的应用前景。已报道的大多数超表面一旦结构设计完成, 一般难以实时调整。可调材料的出现, 使复合超表面拥有了更广阔的应用空间。2020 年, Huang 等^[15]研究了一种基于二氧化钒 (VO_2) 图案的双宽带有源可控太赫兹吸收器, 利用热控制来使 VO_2 相变, 吸收率从 20% 连续调节至 90%。2021 年, 杨朝晖等^[16]提出一种反射式带宽可调极化转换器, 通过使 VO_2 相变, 实现了对太赫兹波极化的动态调控。杨森等^[17]提出一种基于金属线结构的动态可切换双频太赫兹吸收器, 通过调节嵌入在金属线结构中的光敏硅和铱的绝缘或导通状态, 该吸收器可在不改变结构的前提下在 3 个双频完美吸收态之间自由切换。上述研究中, 可调材料只被用于调节器件的谐振频率或带宽振幅, 功能单一。近年来, 可调材料逐渐被用于超表面结构的复合设计, 以实现超表面多功能切换。例如: Qu 等^[18]设计了一种双极化石墨烯基多功能器件, 通过改变嵌入底部金属层的石墨烯环化学势, 实现吸收和透射切换; Yang 等^[19]设计了基于 VO_2 的多功能可重构

超表面, 可实现反射光束分裂、反射聚焦、涡流光束控制和窄带吸收功能动态切换; 杨森等^[19]提出一种温度电压双可控的双功能超表面, 通过调控超表面中 VO_2 和石墨烯的导电特性实现对极化转换和吸收功能的切换。在上述研究中, 可调材料均被嵌入金属图案中, 无疑增加了结构的复杂度及其制作难度, 并且 VO_2 、石墨烯等可调材料需要特别敏感的温度或供电条件, 在实际应用中具有一定难度^[20-21]。光敏硅是一种光可调材料, 其电导率随着泵浦光能量变化, 且调控方式简单, 因此受到了广泛关注。另外, 已有的大多数超表面研究只探讨了可调材料绝缘与导通两种状态, 这种方式限制了功能的多样性, 而光敏硅可以连续调节电导率来产生多种编码状态, 从而拓展功能。

本文设计了一种基于光敏硅图案的可重构超表面。该超表面的结构十分简单, 无须改变单元的形状、大小或方向, 而是利用光控连续调节光敏硅的电导率, 在太赫兹波段实现线-线极化转换、线-圆极化转换、宽带吸收、近场成像、分束等功能, 使太赫兹多功能器件的调节方式更加简便。

2 结构设计

可重构超表面结构如图 1(a) 所示, 单元结构及尺寸参数如图 1(b)、(c) 所示。该超表面单元结构由三层材料组成, 其中: 顶层为由 $0.2 \mu\text{m}$ 厚的光敏硅构成

收稿日期: 2022-11-30; 修回日期: 2022-12-25; 录用日期: 2023-02-09; 网络首发日期: 2023-02-19

基金项目: 国家自然科学基金(61871355, 61831012, 62271460)、浙江省重点研发项目(2021C03153, 2022C03166)

通信作者: *lijsh@cju.edu.cn

的双开口 C 环结构,大 C 环的外半径 $r_{\text{large}}=14\ \mu\text{m}$ 、宽度为 $4\ \mu\text{m}$,小 C 环的外半径 $r_{\text{small}}=8\ \mu\text{m}$ 、宽度为 $4.5\ \mu\text{m}$,两环开口均关于单元对角线对称,开口宽度分别为 $a=6\ \mu\text{m}$ 和 $b=3\ \mu\text{m}$;中间介质层为二氧化硅,其介电常数为 3.9,厚度 $h=10\ \mu\text{m}$;底层为 $0.5\ \mu\text{m}$ 厚的金属铜,单元周期 $P=40\ \mu\text{m}$ 。光敏硅的介电常数为 11.7,其电导率会随着泵浦光能量变化,当光照能量增加时,半导体内的载流子浓度也会增大,从而达到调控电导率的目的。光敏硅电导率 σ 和泵浦光功率 I 之间的关

系^[22]为 $\sigma=4.863\times 10^{-4}\times I^2+0.1856\times I+1.569$ 。在无泵浦激励时,光敏硅的电导率为 0;当泵浦光功率为 $600\ \mu\text{J}/\text{cm}^2$ 时,电导率为 $2.5\times 10^5\ \text{S}/\text{m}$;当泵浦光功率为 $790\ \mu\text{J}/\text{cm}^2$ 时,电导率为 $5.0\times 10^5\ \text{S}/\text{m}$ 。为了方便描述,本文将光敏硅电导率为 0 时编码为 0,电导率为 $5.0\times 10^5\ \text{S}/\text{m}$ 时编码为 1,电导率为 $2.5\times 10^5\ \text{S}/\text{m}$ 时编码为 2,所涉及的数字编码的 5 种状态为 00、01、10、11、22,如表 1 所示。

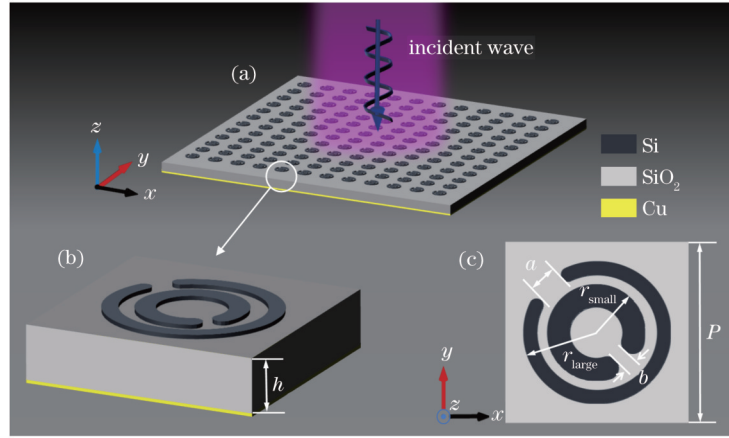


图 1 可重构超表面及其单元结构。(a)超表面三维示意图;(b)单元三维示意图;(c)单元俯视图

Fig. 1 Reconfigurable metasurface and its unit structure. (a) Three-dimensional diagram of metasurface; (b) three-dimensional diagram of unit; (c) top view of unit

表 1 不同状态光敏硅的参数和模型

Table 1 Detailed parameters and models of photosensitive silicon in different states

State	Conductivity of small C-ring / ($\text{S}\cdot\text{m}^{-1}$)	Conductivity of large C-ring / ($\text{S}\cdot\text{m}^{-1}$)	Model
00	0	0	
01	5.0×10^5	0	
10	0	5.0×10^5	
11	5.0×10^5	5.0×10^5	
22	2.5×10^5	2.5×10^5	

3 结果仿真与器件性能分析

3.1 极化转换

当光敏硅处于状态 10 时,该结构表现为线-线极

化转换器。从图 2(a)可以看到,在 $2.10\sim 3.15\ \text{THz}$ 频率范围内,交叉极化反射系数 r_{yx} 和 r_{xy} 在 0.9 以上,共极化反射系数 r_{xx} 和 r_{yy} 则低于 0.3,这表明在此频率范围入射的 y 极化波转换为 x 极化波,入射的 x 极化波将转换为 y 极化波。为了更好地解释线性极化转换的性能,引用反射式极化转换率(PCR)计算公式^[23],可表示为

$$\eta_{\text{PCR},x} = |r_{yx}|^2 / (|r_{yx}|^2 + |r_{xx}|^2), \quad (1)$$

$$\eta_{\text{PCR},y} = |r_{xy}|^2 / (|r_{xy}|^2 + |r_{yy}|^2), \quad (2)$$

式中: $\eta_{\text{PCR},x}$ 、 $\eta_{\text{PCR},y}$ 分别为 x 和 y 方向的 PCR。从图 2(b)可以看到,在该频率范围内 PCR 大于 90%,该结构具有良好的宽带线性极化转换性能。图 3 所示为 $2.30\ \text{THz}$ 和 $2.90\ \text{THz}$ 两个频点处光敏硅结构和金属层的电流分布。极化波在 $2.30\ \text{THz}$ 处光敏硅大环等效电流与金属层的等效电流(黑色)方向大致相反,即在 $2.30\ \text{THz}$ 处仅形成磁共振,如图 3(a)所示;在 $2.90\ \text{THz}$ 处光敏硅大环表面电流存在两个方向,但都与金属板表面电流近似垂直,因此将电流流向分解为水平和垂直两个方向,光敏硅大环与金属板在水平方向上同时存在同向与反向电流,即形成电偶共振和磁偶共振,如图 3(b)所示,表明 $2.90\ \text{THz}$ 处的线-线极化转换功能主要由光敏硅大环与底部金属板之间的磁共振和电共振共同决定。

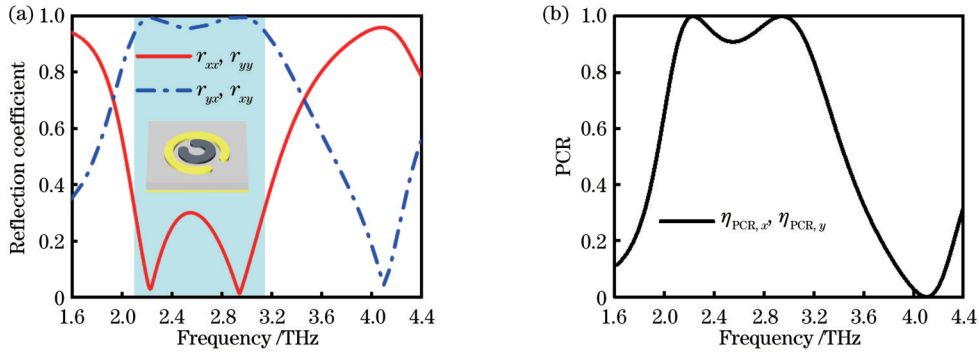


图 2 入射太赫兹波的反射系数及对应的 PCR。(a) x 极化波和 y 极化波垂直入射时的反射系数; (b) PCR

Fig. 2 Reflection coefficient of incident terahertz wave and corresponding PCR. (a) Reflection coefficient of x -polarized wave and y -polarized wave at normal incidence; (b) PCR

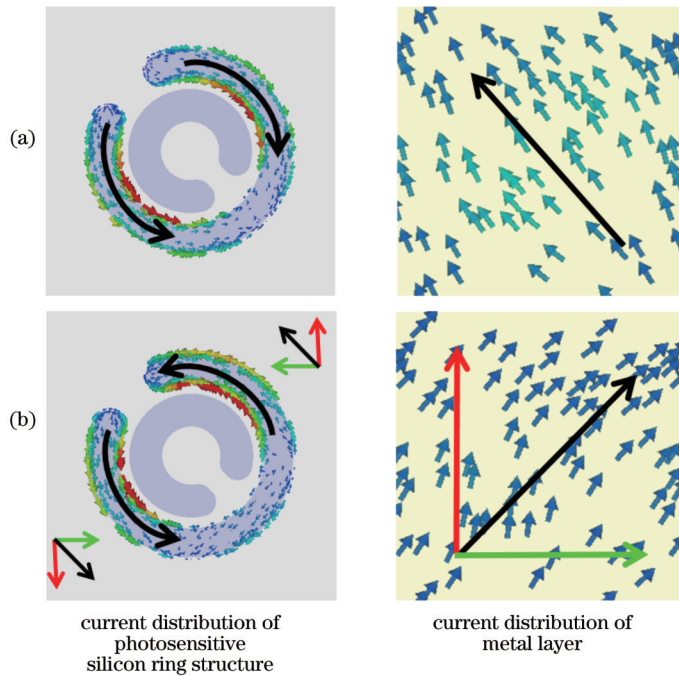


图 3 极化波垂直入射时光敏硅环形结构和金属层的电流分布。(a) $f=2.30$ THz; (b) $f=2.90$ THz

Fig. 3 Current distribution of photosensitive silicon ring structure and metal layer when polarization wave is perpendicular incident. (a) $f=2.30$ THz; (b) $f=2.90$ THz

当光敏硅处于状态 01 时, 所设计超表面表现为线-圆极化转换器。图 4(a) 所示为太赫兹波垂直入射时 x 极化波或 y 极化波垂直入射时的反射系数, 可以看到, 在 2.33~2.47 THz 和 2.78~4.40 THz 两个频率范围内, 共极化反射系数与交叉极化反射系数相近。从图 4(b) 所示的反射波 x 分量和 y 分量的相位差可以看出: 在 2.33~2.47 THz 频率范围内, 共极化反射与交叉极化反射之间的相位差 $\Delta\varphi$ 接近 270° , 即反射波为左圆极化波 (LCP); 在 2.78~4.40 THz 频率范围内, 两者的相位差 $\Delta\varphi$ 为 90° 或 -270° , 即反射波为右圆极化波 (RCP)。

引入斯托克斯参数 (I 、 Q 、 U 、 V) 可以更好地解释该极化转换器性能^[24-25], 即

$$\begin{cases} I = |r_{xy}|^2 + |r_{yx}|^2 \\ Q = |r_{yy}|^2 - |r_{xx}|^2 \\ U = 2|r_{xy}||r_{yy}| \cos \Delta\varphi \\ V = 2|r_{xy}||r_{yy}| \sin \Delta\varphi \end{cases}, \quad (3)$$

式中: $\Delta\varphi = \varphi_{yx} - \varphi_{xx}$ 引入椭圆率 $\chi = U/I$; 当 $\chi = 1$ 时, 反射波为右圆极化波; 当 $\chi = -1$ 时, 反射波为左圆极化波。从图 5(a) 可以看到: 在 2.33~2.47 THz 频率范围内, 椭圆率接近 -1 ; 在 2.78~4.40 THz 频率范围内, 椭圆率接近 1 。另外, 轴比 (ζ_{AR}) 也可以直观地表现转换性能^[26]:

$$\zeta_{AR} = 10 \log(|r_{yx}|/|r_{xx}|). \quad (4)$$

图 5(b) 所示为该线-圆极化转换器的轴比, 可以看

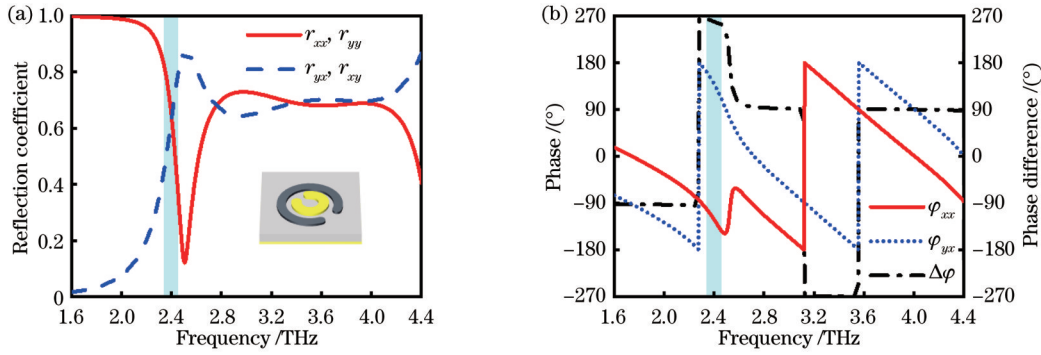


图 4 太赫兹波垂直入射时的反射系数及相位差。(a) x 极化波或 y 极化波垂直入射时的反射系数;(b)反射波 x 分量和 y 分量的相位差

Fig. 4 Reflection coefficient and phase difference of terahertz wave at vertical incidence. (a) Reflection coefficient of x -polarized wave or y -polarized wave at vertical incidence; (b) phase difference of x -component and y -component of reflected wave

到:在 2.40 THz 处和 2.70~4.20 THz 范围内, ζ_{AR} 接近 0 dB;在 2.34~2.46 THz 和 2.61~4.42 THz 范围内, $\zeta_{AR} < 3$ dB, 相对带宽分别达到 4.9% 和 51.5%。可见,该结构有良好的线-圆转换性能。在 2.40 THz 和 3.40 THz 频率处光敏硅结构和金属层的电流分布

如图 6 所示,因为光敏硅小环等效电流为环形电流,所以小环的部分电流方向与金属板电流方向相同,但部分电流方向相反。由此可见,所设计结构的线-圆极化转换功能主要由光敏硅小环与底部金属板之间的磁共振和电共振共同决定。

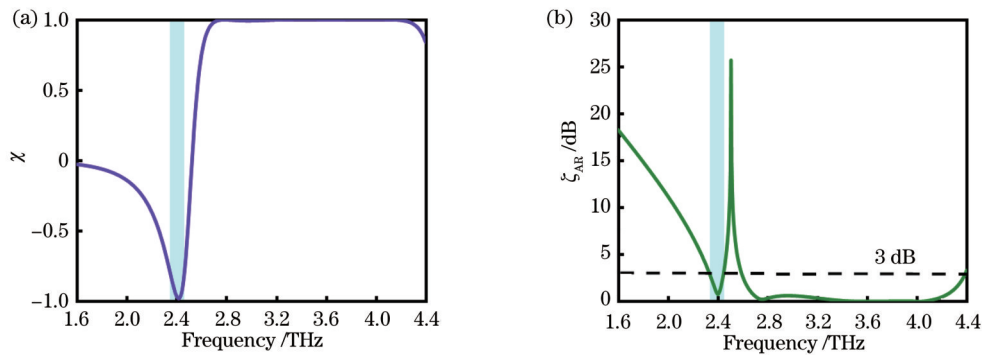


图 5 太赫兹波垂直入射时的椭圆率和轴比。(a) x 极化或 y 极化太赫兹波垂直入射时的椭圆率;(b)轴比

Fig. 5 Ellipticity and axial ratio of terahertz wave at vertical incidence. (a) Ellipticity of x -polarized or y -polarized terahertz wave at vertical incidence; (b) axial ratio

3.2 宽带吸收

当光敏硅为状态 22 时,该结构可作为宽带吸收器。由于存在底部金属板,该结构的透射率可忽略不计,只需要计算反射率(R_{refl})。定义吸收器的吸收率(A)为

$$A = 1 - R_{\text{refl}} = 1 - |r_{yy}|^2 - |r_{xy}|^2 \quad (5)$$

当太赫兹波垂直入射时,该吸收器对极化不敏感,对线极化波和圆极化波具有相同的吸收性能,如图 7 所示,在 2.40~4.60 THz 频率范围内,吸收率大于 90%。

为了更直观地了解该吸收器的工作机制,图 8(a)给出了等效电路模型,两个光敏硅环之间的分布电容存在耦合。由于吸收器的尺寸远小于波长,在准静态模式下通过两个环的感应电流大小相同,该吸收器就可以等效为由外部电动势驱动的 LC 电路,由于光敏

硅为环形,因此电路的总电容由大小不同的电容组成,该电路的谐振频率可以表示为

$$f = \sqrt{\frac{1}{LC\pi^2}} \quad (6)$$

式中: C 表示双环间的总电容值, $C = 2\pi m C_0$, C_0 为单位长度下双环间的电容值,可以近似表示为 $C_0 = \epsilon_0 S/n$, ϵ_0 为真空电容率, S 为双环面积; L 为电路总电感。电路总电容为 $C/4$,这里把该双环结构的电感近似成单环,则 n 为开口圆环的等效宽度, m 为等效半径,如图 8(b)所示。

图 9 所示为在 2.90 THz 和 4.50 THz 两个频率下的完美太赫兹吸收电场分布,可见两个圆形缺口环产生了明显的偶极共振,能量主要集中于缺口附近。图 10 所示为斜入射角度对器件吸收性能的影响,其中:图 10(a)所示为入射角对 TE 波的影响,随着入射

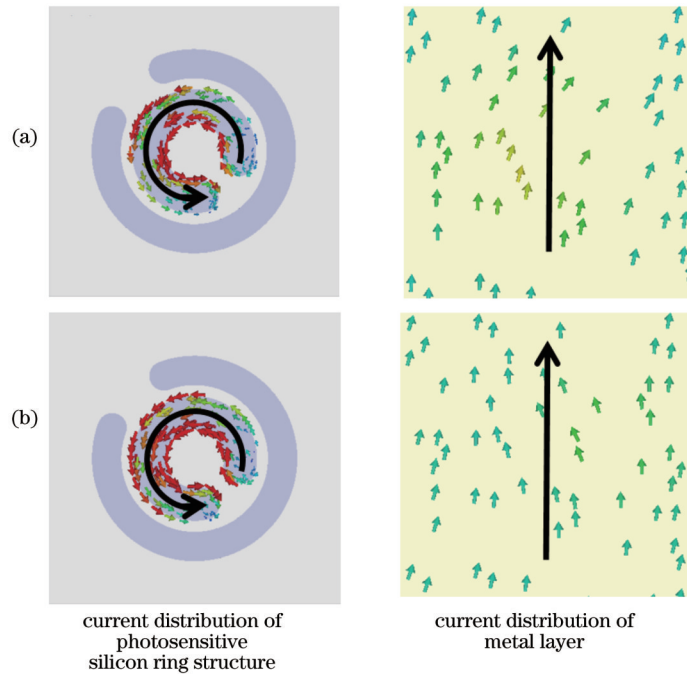


图 6 极化波垂直入射时光敏硅环形结构和金属层的电流分布。(a) $f=2.40$ THz; (b) $f=3.40$ THz

Fig. 6 Current distribution of photosensitive silicon ring structure and metal layer when polarization wave is perpendicular incident. (a) $f=2.40$ THz; (b) $f=3.40$ THz

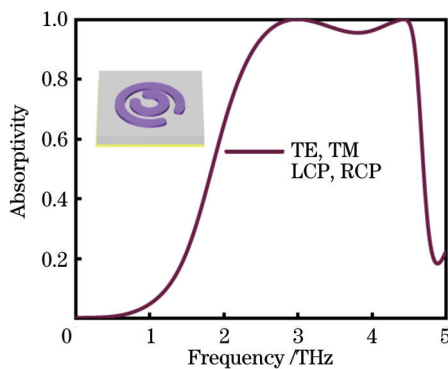


图 7 所设计器件对太赫兹波的吸收率

Fig. 7 Absorption rate of terahertz wave in the designed device
角度逐渐增大,吸收峰出现轻微红移,且当入射角达到 70° 时,吸收率仍保持在 80% 以上,表明超表面具有良好的广角吸收性能;图 10(b) 所示为入射角对 TM 波

的影响,当入射角不为 0° 时, TM 波的吸收率与 TE 波有较大差别,且随着入射角逐渐增大,吸收峰逐渐变窄。

3.3 近场成像

状态 00 和 22 的光敏硅在 $2.80\sim 3.00$ THz 频率范围内拥有较大的反射幅度差和较小的相位差,本文利用这一特性进行近场成像仿真实验。如图 11(a) 所示,两种状态的光敏硅在 $2.80\sim 3.00$ THz 频率范围内的反射幅度差接近 0.9;从图 11(b) 可以看出,该范围内二者的相位差比较小,只有 50° 左右。基于以上特性,分别对“P”和“+”图案进行成像分析,两种单元结构分别排布在图案内部和图案外围,具体排布如图 12(a) 所示。在 $2.80\sim 3.00$ THz 频率范围内,所设计的超表面阵列都取得较好的成像效果。图 12(b) 展示了频率为 2.90 THz 时,距离超表面 $10\ \mu\text{m}$ 处的成像

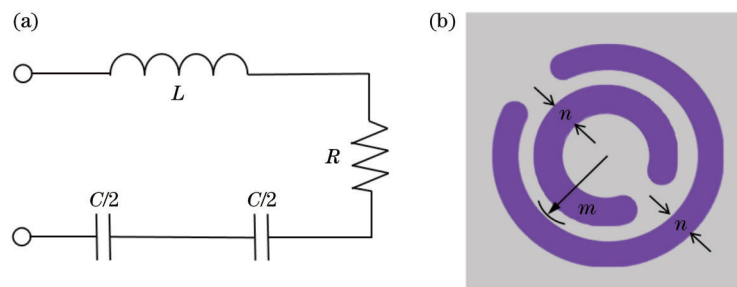


图 8 所设计结构作为吸收器时的等效电路模型及等效结构参数。(a) 等效电路模型; (b) 结构单元等效参数

Fig. 8 Equivalent circuit model and equivalent structural parameters of the proposed structure as an absorber. (a) Equivalent circuit model; (b) structural element equivalent parameter

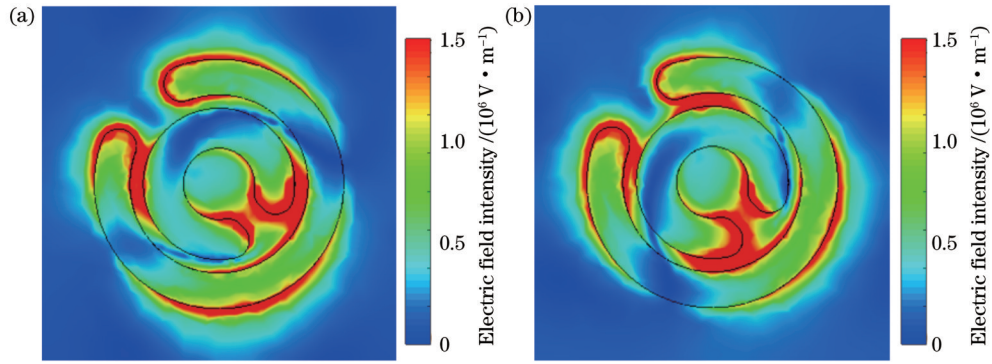


图 9 不同频率时的表面电场分布。(a) $f=2.90$ THz; (b) $f=4.50$ THz

Fig. 9 Surface electric field distribution under different frequencies. (a) $f=2.90$ THz; (b) $f=4.50$ THz

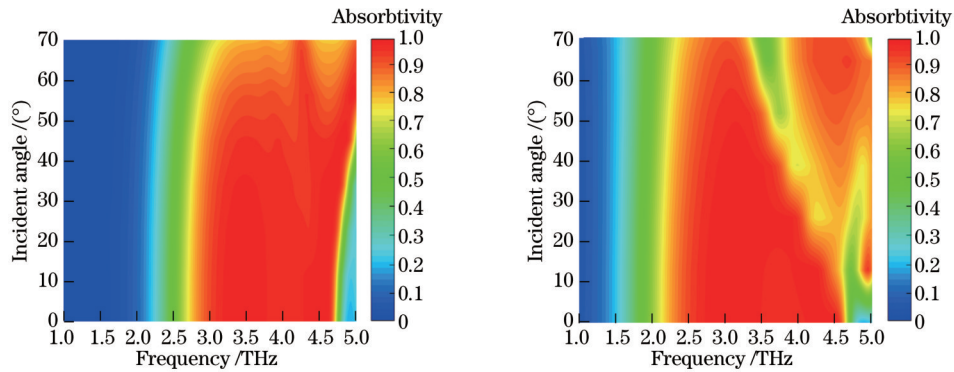


图 10 入射角对吸收性能的影响。(a) TE 波入射时吸收率随入射角的变化; (b) TM 波入射时吸收率随入射角的变化

Fig. 10 Effect of incident angle on absorption performance. (a) Change of absorptivity with incident angle under TE wave incidence; (b) change of absorptivity with incident angle under TM wave incidence

结果,可以看出图案内部与图案外围的能量具有很大的差异。

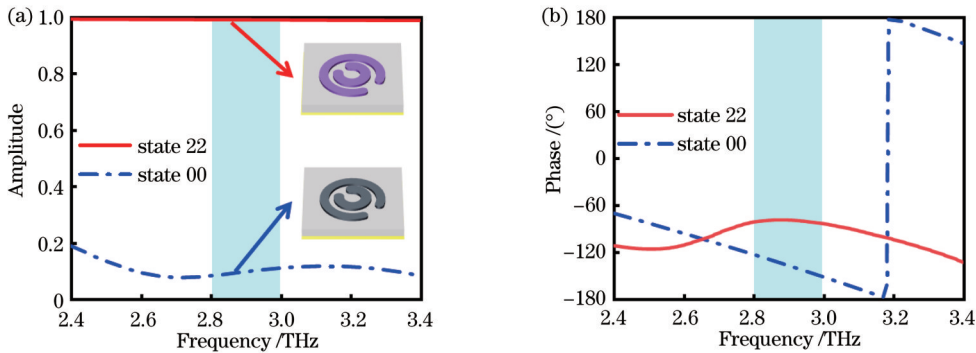


图 11 太赫兹波垂直入射时,状态 00、22 光敏硅的反射幅度和相位。(a) 幅度; (b) 相位

Fig. 11 Reflection amplitude and phase of photosensitive silicon in 00 and 22 states when terahertz wave is incident vertically.

(a) Amplitude; (b) phase

3.4 分束

从图 13 可以看到,状态 10 和 00 的光敏硅在 3.3 THz 处拥有 180° 相位差和 0.8 以上的反射幅度,满足 1 bit 编码超表面的编码状态要求。将状态 10 的光

敏硅单元重新编码为 0 (红色), 状态 00 的光敏硅重新编码为 1 (蓝色)。当太赫兹波垂直入射到编码超表面时,远场方向函数^[27]为

$$f(\theta, \varphi) = f_c(\theta, \varphi) \sum_{m=1}^M \sum_{n=1}^N \exp \left\{ -i \left[\varphi(m, n) + KD_x \sin \theta \left(m - \frac{1}{2} \right) \cos \varphi + KD_y \left(n - \frac{1}{2} \right) \cos \varphi \sin \theta \right] \right\}, \quad (7)$$

式中: D_x 和 D_y 分别表示栅格的长度和宽度; $\varphi(m, n)$ 为栅格的散射相位; θ 和 φ 为任意方向上的俯仰角和方位角;

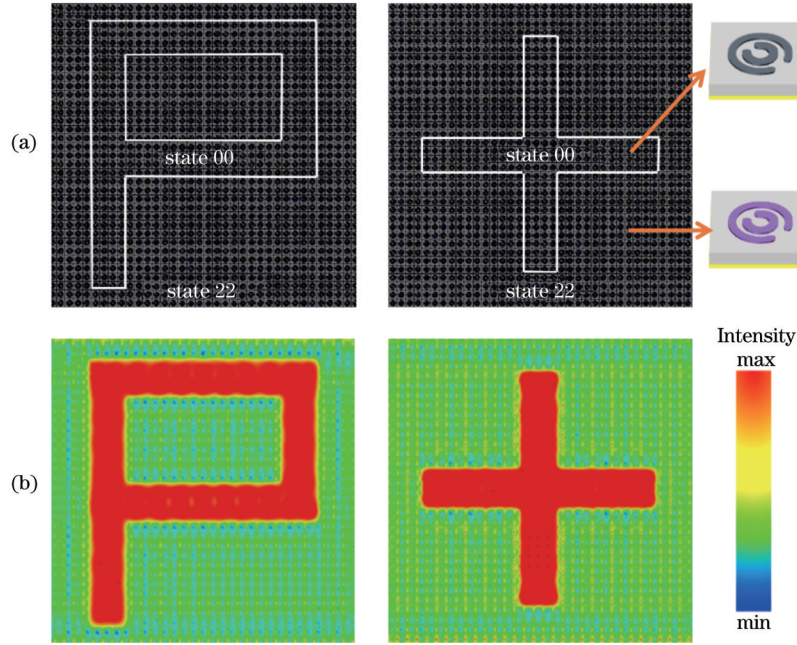


图 12 阵列排布图和成像效果。(a)状态 00、22 的光敏硅排布情况;(b)频率为 2.90 THz、太赫兹波垂直入射、观测距离为 10 μm 时的成像效果

Fig. 12 Array layout and imaging effect. (a) Arrangement of photosensitive silicon in 00 and 22 states; (b) imaging effect when the frequency is 2.90 THz, terahertz wave is vertically incident, and the observation distance is 10 μm

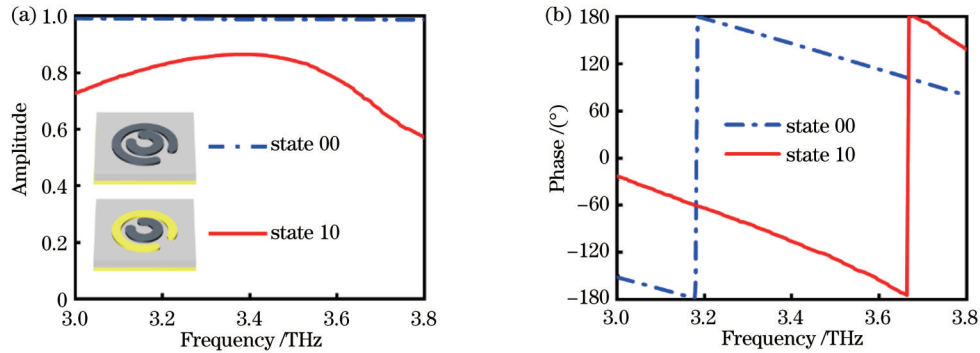


图 13 太赫兹波垂直入射时,状态 10、00 光敏硅的反射幅度和相位。(a)幅度;(b)相位

Fig. 13 Reflection amplitude and phase of photosensitive silicon in 10 and 00 states when terahertz wave is incident vertically. (a) Amplitude; (b) phase

$f_e(\theta, \varphi)$ 为栅格的方向函数。由于 0 和 1 单元结构的相位差为 180° , 散射特性相消, 因此 $f_e(\theta, \varphi)$ 的辐射特性可以忽略不计, 式(7)可进一步简化为

$$f(\theta, \varphi) = \sum_{m=1}^M \exp \left\{ -i \left[KD_x \left(m - \frac{1}{2} \right) \sin \theta \cos \theta + m\pi \right] \right\} \sum_{n=1}^N \exp \left\{ -i \left[KD_y \left(n - \frac{1}{2} \right) + n\pi \right] \right\}. \quad (8)$$

若 $f(\theta, \varphi)$ 取得最大值, 需要满足以下条件

$$\begin{cases} \varphi = \pm \arctan \frac{D_x}{D_y} \\ \varphi = \pi \pm \arctan \frac{D_x}{D_y} \end{cases}, \quad (9)$$

$$\theta = \arcsin \left(\frac{\lambda}{2} \sqrt{\frac{1}{D_y^2} + \frac{1}{D_x^2}} \right) = \arcsin \left(\frac{\lambda}{\Gamma} \right), \quad (10)$$

式中: λ 为自由空间的工作波长; Γ 为编码超表面一个梯度周期的长度。将 0 和 1 单元按“00001111.../00001111...”的周期性编码方式进行排布, 组成 32×32 阵列, 当频率为 3.3 THz 时, 太赫兹波垂直入射到超表面时被分为 2 束反射波束, 通过式(9)和(10)可以计算得到反射波束方向, 俯仰角 $\theta = 16.2^\circ$, 方位角 φ 为 0° 和 180° 。图 14(a) 为其三维远场图, 图 14(b)、(c) 为归一化二维远场图和二维电场图。将 0 和 1 单元按

“00001111.../11110000...”的编码方式进行排布,组成 32×32 阵列,当频率为 3.3 THz 时,垂直入射的太赫兹波被超表面反射为 4 束波束,经计算得到俯仰角 θ

为 23.6° ,方位角 φ 分别为 45° 、 135° 、 225° 和 315° 。图 15 (a) 为其三维远场图,图 15 (b)、(c) 为归一化二维远场图和二维电场图。

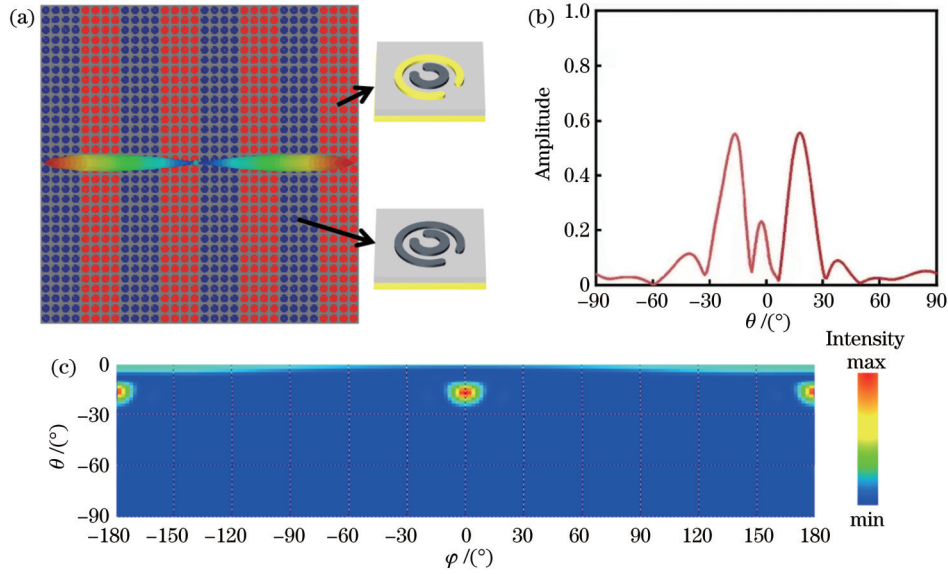


图 14 太赫兹波垂直入射时,以 0-0、0-1 为周期沿 x 方向排列的 1 bit 编码超表面在 3.3 THz 处的分束效果。(a) 三维远场散射图; (b) 归一化二维远场图; (c) 二维电场图
 Fig. 14 Beam splitting effect at 3.3 THz of 1 bit coded metasurface arranged along the x direction with period of 0-0 and 0-1 when terahertz wave is incident vertically. (a) Three-dimensional far field scattering diagram; (b) normalized two-dimensional far field diagram; (c) two-dimensional electric field diagram

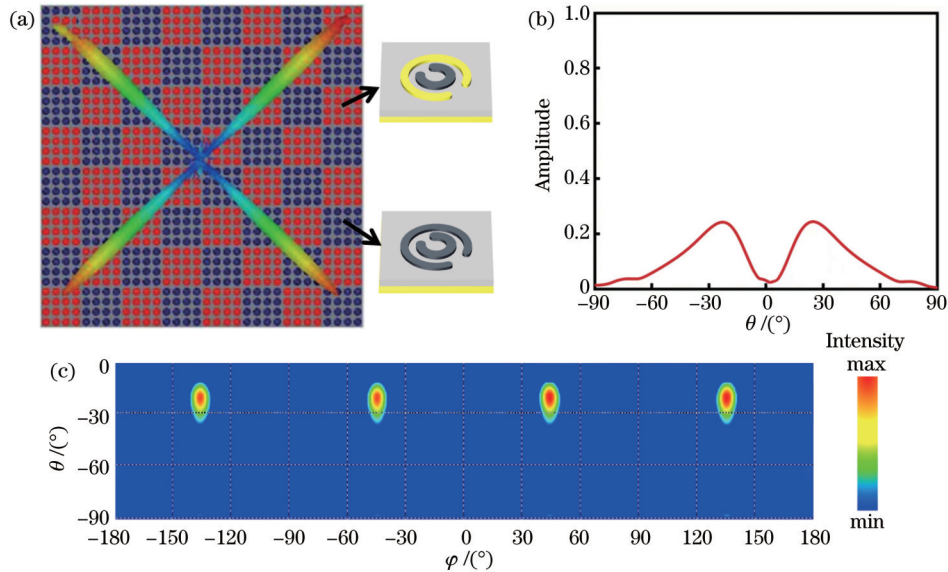


图 15 太赫兹波垂直入射时,以 0-0、0-1 为周期棋盘式排列的 1 bit 编码超表面在 3.3 THz 处的分束效果。(a) 三维远场散射图; (b) 归一化二维远场图; (c) 二维电场图
 Fig. 15 Beam splitting effect at 3.3 THz of 1 bit coded metasurface arranged in chessboard pattern with period of 0-0 and 0-1 when terahertz wave is incident vertically. (a) Three-dimensional far field scattering diagram; (b) normalized two-dimensional far field diagram; (c) two-dimensional electric field diagram

3.5 性能对比

在超表面研究领域,能够实现吸收和极化转换等功能的可重构超表面已引起广泛关注。本研究与其他研究之间的比较如表 2 所示:He 等^[28]提出一种基于二

极管嵌入金属图层的多功能超表面,实现了极化转换、全反射功能的切换,但二极管只有导通和断开两种状态,导致该超表面的功能受到局限;Wang 等^[29]提出一种基于石墨烯的动态可调谐等离子体诱导透明(PIT)

结构,利用 VO₂衬底层的相变特性能够使超表面在 PIT 和完美吸收之间实现动态切换,而石墨烯和 VO₂的非嵌入式设计使结构更加简化,但 VO₂只具有绝缘和金属两种状态,导致器件的功能多样性受到限制;Yang 等^[30]提出一种基于 VO₂嵌入多层结构的全空间太赫兹超表面,可以实现透射或反射模式下的分束、多涡旋、聚焦功能。虽然可调材料相变特性结合全空间

可使功能更加丰富,但 VO₂嵌入层数过多也会导致结构较为复杂,难以加工。

综上所述,所设计的结构图案完全由光敏硅构成,明显降低了图案复杂度和器件制造难度。同时,利用光敏硅电导率连续可调的特性,产生多种编码状态,使超表面功能更加强大,相比于功能单一的超表面在集成度等方面具有更大优势。

表 2 本研究与其他研究对比

Table 2 Comparison of this study with other studies

Ref.	Accommodation mode	Function
[28]	Embedded diode	Linear-to-circular polarization conversion and total reflection
[29]	Graphene pattern, VO ₂ substrate layer	PIT and absorption
[30]	Embedded VO ₂	Beam splitting, vortex beam, and focusing
This paper	Photosensitive silicon pattern	Linear-to-circular polarization conversion, linear-to-linear polarization conversion, absorption, near-field imaging, and beam splitting

4 结 论

利用光敏硅双 C 环结构设计可重构超表面,实现了对极化转换、宽带吸收、近场成像、分束等功能的切换。当光敏硅状态为 10 时,该超表面可实现 2.10~3.15 THz 频率范围内 PCR 大于 90% 的线-线偏振转换;当光敏硅状态为 01 时,可实现线-圆偏振转换,在 2.33~2.47 THz 频段内反射波为左圆极化波,在 2.78~4.40 THz 频段内反射波为右圆极化波;若将光敏硅调节为状态 22,超表面表现为吸收器,可以实现 2.40~4.60 THz 频率范围内吸收率大于 90%,且该吸收器具有良好的广角吸收性能;将状态 00 和 22 的两个具有较大反射幅度差和较小反射相位差的单元进行编码,可实现近场成像,在 2.80~3.00 THz 范围内,距离超表面 10 μm 处的成像效果都较为理想;将状态 10 和 00 的两个具有 180° 反射相位差和较高反射幅值的单元进行编码,入射太赫兹波被分为 2 束或 4 束,其中 2 束波的俯仰角为 18°,4 束波的俯仰角为 32.5°。研究结果表明,利用外部条件控制可调材料,可实现超表面功能的灵活切换,同时使得多功能器件调控更加灵活,可实现功能调控的范围更广,在太赫兹调制、隐身技术、通信系统等方面具有良好的应用前景。

参 考 文 献

- [1] 鲍迪,沈晓鹏,崔铁军.太赫兹人工电磁媒质研究进展[J].物理学报,2015,64(22):228701.
Bao D, Shen X P, Cui T J. Progress of terahertz metamaterials[J]. Acta Physica Sinica, 2015, 64(22): 228701.
- [2] Yu S X, Liu H X, Li L. Design of near-field focused metasurface for high-efficient wireless power transfer with multifocus characteristics[J]. IEEE Transactions on Industrial Electronics, 2019, 66(5): 3993-4002.
- [3] Chen K, Feng Y J, Monticone F, et al. A reconfigurable active Huygens' metalens[J]. Advanced Materials, 2017, 29(17): 1606422.

- [4] Fan Y X, Qian Y X, Yin S, et al. Multi-band tunable terahertz bandpass filter based on vanadium dioxide hybrid metamaterial[J]. Materials Research Express, 2019, 6(5): 055809.
- [5] Liu W W, Dai Z J, Yang J, et al. Ultrabroad and angle tunable THz filter based on multiplexed metallic bar resonators[J]. IEEE Photonics Technology Letters, 2018, 30(24): 2103-2106.
- [6] Masyukov M, Grebenchukov A N, Litvinov E A, et al. Phototunable terahertz absorber based on intercalated few-layer graphene[J]. Journal of Optics, 2020, 22(9): 095105.
- [7] He Z D, Wu L W, Liu Y, et al. Ultrawide bandwidth and large-angle electromagnetic wave absorption based on triple-nested helix metamaterial absorbers[J]. Journal of Applied Physics, 2020, 127(17): 174901.
- [8] Huang J X, Fu T, Li H O, et al. A reconfigurable terahertz polarization converter based on metal-graphene hybrid metasurface[J]. Chinese Optics Letters, 2020, 18(1): 013102.
- [9] Wang H Y, Zhang Z Y, Zhao K, et al. Independent phase manipulation of co- and cross-polarizations with all-dielectric metasurface[J]. Chinese Optics Letters, 2021, 19(5): 053601.
- [10] Zhou G C, Dai P H, Wu J B, et al. Broadband and high modulation-depth THz modulator using low bias controlled VO₂-integrated metasurface[J]. Optics Express, 2017, 25(15): 17322-17328.
- [11] Ma Z J, Hanham S M, Gong Y D, et al. All-dielectric reflective half-wave plate metasurface based on the anisotropic excitation of electric and magnetic dipole resonances[J]. Optics Letters, 2018, 43(4): 911-914.
- [12] Yang L J, Li J S, Yan D X. Switchable multi-function device based on reconfiguration metasurface in terahertz region[J]. Optics Communications, 2022, 516: 128234.
- [13] Lin Z, Pestourie R, Roques-Carnes C, et al. End-to-end metasurface inverse design for single-shot multi-channel imaging[J]. Optics Express, 2022, 30(16): 28358-28370.
- [14] Li H, Li Y B, Shen J L, et al. Low-profile electromagnetic holography by using coding Fabry-Perot type metasurface with in-plane feeding[J]. Advanced Optical Materials, 2020, 8(9): 1902057.
- [15] Huang J, Li J N, Yang Y, et al. Active controllable dual broadband terahertz absorber based on hybrid metamaterials with vanadium dioxide[J]. Optics Express, 2020, 28(5): 7018-7027.
- [16] 杨朝晖,江明珠,刘永琛,等.基于二氧化钒复合超表面的太赫兹带宽可调极化转换器[J].中国激光,2021,48(17): 1714001.
Yang Z H, Jiang M Z, Liu Y C, et al. Tunable-bandwidth

- terahertz polarization converter based on a vanadium dioxide hybrid metasurface[J]. Chinese Journal of Lasers, 2021, 48(17): 1714001.
- [17] 杨森, 袁苏, 王佳云. 一种光激发可切换的双频太赫兹超材料吸收器[J]. 光学学报, 2021, 41(2): 0216001.
Yang S, Yuan S, Wang J Y. Light-excited and switchable dual-band terahertz metamaterial absorber[J]. Acta Optica Sinica, 2021, 41(2): 0216001.
- [18] Qu M J, Chang T Y, Guo G, et al. Design of graphene-based dual-polarized switchable absorber/absorber at terahertz[J]. IEEE Access, 2020, 8: 127220-127225.
- [19] 杨森, 王佳云, 张婷, 等. 温度电压双可控宽带太赫兹极化转换/吸收超表面[J]. 光学学报, 2022, 42(8): 0824001.
Yang S, Wang J Y, Zhang T, et al. Temperature-voltage bi-controllable broadband terahertz polarization conversion/absorption metasurface[J]. Acta Optica Sinica, 2022, 42(8): 0824001.
- [20] He B, Fan J P, Cheng Y, et al. Thermally tunable terahertz vortex beam generator based on an InSb metasurface[J]. Journal of the Optical Society of America B, 2021, 38(5): 1518-1524.
- [21] Cheng Y Z, Liu J Q, Chen F, et al. Optically switchable broadband metasurface absorber based on square ring shaped photoconductive silicon for terahertz waves[J]. Physics Letters A, 2021, 402: 127345.
- [22] Cheng Y Z, Gong R Z, Zhao J C. A photoexcited switchable perfect metamaterial absorber/reflector with polarization-independent and wide-angle for terahertz waves[J]. Optical Materials, 2016, 62: 28-33.
- [23] Murtaza M, Rashid A, Tahir F A. A highly efficient low-cost reflective anisotropic metasurface for linear to linearly cross- and circular-polarization conversion[J]. Microwave and Optical Technology Letters, 2021, 63(5): 1346-1353.
- [24] Cong L Q, Xu N N, Gu J Q, et al. Highly flexible broadband terahertz metamaterial quarter-wave plate[J]. Laser & Photonics Reviews, 2014, 8(4): 626-632.
- [25] He J W, Xie Z W, Wang S, et al. Terahertz polarization modulator based on metasurface[J]. Journal of Optics, 2015, 17(10): 105107.
- [26] Qiao Q, Wang Y K, Yang G F, et al. Broadband of linear-to-linear and double-band of linear-to-circular polarization converter based on a graphene sheet with a π -shaped hollow array[J]. Optical Materials Express, 2021, 11(9): 2952-2965.
- [27] Li Y, Li H Y, Wang Y W, et al. A novel switchable absorber/linear converter based on active metasurface and its application [J]. IEEE Transactions on Antennas and Propagation, 2020, 68(11): 7688-7693.
- [28] He J H, Wang S Q, Li X W, et al. A broadband reconfigurable linear-to-circular polarizer/reflector based on PIN diodes[J]. Physica Scripta, 2021, 96(12): 125846.
- [29] Wang S Z, Liu H Q, Tang J, et al. Tunable and switchable bifunctional meta-surface for plasmon-induced transparency and perfect absorption[J]. Optical Materials Express, 2022, 12(2): 560-572.
- [30] Yang L J, Li J S. Full-space terahertz regulation metasurface[J]. Optical Engineering, 2022, 61(4): 047105.

Multifunctional Reconfigurable Metasurface Based on Photosensitive Silicon

Ren Jiahui, Li Jiusheng*

Center for THz Research, China Jiliang University, Hangzhou 310018, Zhejiang, China

Abstract

Objective Tunability is an important requirement for metasurface application. In recent years, adjustable materials have been gradually used in the composite design of metasurface structures to achieve multi-functional switching. However, most of the existing relevant studies still have some shortcomings. First, the adjustable material is usually embedded in the metal pattern, which undoubtedly increases the complexity and manufacturing difficulty of the structure. Second, commonly used adjustable materials such as vanadium dioxide and graphene require particularly sensitive temperature environments or feeding conditions, and the temperature and bias voltage should be considered in the design and application, which not only complicates the production process but also brings a certain degree of difficulty to the practical application. Third, most of the reported metasurfaces only discuss the insulating and metallic states of adjustable materials, which limits the diversity of functions. Photosensitive silicon is a kind of light-adjustable material, and its conductivity changes with the change in pump light energy. It has attracted wide attention because of its simple regulation mode. Moreover, photosensitive silicon can continuously adjust the conductivity to generate a variety of coding states, so as to expand its functions. In this paper, a reconfigurable metasurface based on a photosensitive silicon pattern is designed. The metasurface does not need to change the shape, size, or direction of the unit but uses the optical control to continuously adjust the conductivity of photosensitive silicon, so as to realize several functions in the terahertz band, such as linear-to-linear polarization conversion, linear-to-circular polarization conversion, broadband absorption, near-field imaging, and beam splitting, which makes the regulation mode of multifunctional terahertz devices more convenient.

Methods In this study, the pattern of the unit structure is completely composed of photosensitive silicon, and the processing technology of silicon-based metasurface is very mature, which will greatly reduce the production difficulty. The

conductivity of photosensitive silicon varies with the light energy pumped. When the light energy increases, the carrier concentration in the semiconductor also increases. By adjusting the conductivity of the two photosensitive silicon rings, five coding states can be obtained, so as to encode metasurfaces with different functions. In this paper, the polarization conversion and absorption function can be realized by using the resonance between the photosensitive silicon and the metal plate or between the double rings. The amplitude difference of different state units can be used for imaging, and the phase difference can be used for beam splitting.

Results and Discussions The designed metasurface can generate multiple coding states by continuously adjusting the conductivity of two photosensitive silicon rings (Table 1), so as to realize multifunctional switching in the terahertz band. When the conductivity of the large and small C-rings is 5.0×10^5 S/m and 0 S/m, respectively, the designed metasurface is presented as a linear-to-linear polarization converter (Fig. 2), and the polarization conversion ratio (PCR) in the range of 2.10–3.15 THz is greater than 90%. When the conductivity of the large and small C-rings is changed to 0 S/m and 5.0×10^5 S/m, respectively, the structure behaves as a linear-to-circular polarization converter (Fig. 4) in the range of 2.33–2.47 THz and 2.78–4.40 THz. When the conductivity of the large and small C-rings changes to 2.5×10^5 S/m at the same time, the structure is transformed into an absorber (Fig. 7) with an absorption rate of more than 90% in the range of 2.40–4.60 THz. By encoding the cells with the conductivity of both large and small C-rings of 0 S/m and 2.5×10^5 S/m, the structure achieves near-field imaging (Fig. 12) in the range of 2.80–3.00 THz. The cells with the conductivity of 5.0×10^5 S/m and 0 S/m for the large and small C-rings and those with the conductivity of 0 S/m for the large and small C-rings are periodically coded, and this structure can realize two beam splitting (Fig. 14) and four beam splitting (Fig. 15) of the terahertz wave. The results show that the metasurface can be reconstructed by changing the external illumination conditions, and a variety of terahertz control functions can be obtained.

Conclusions In this paper, the reconfigurable metasurface designed by the photosensitive silicon double C-rings structure realizes the switching of several functions, such as linear-to-linear polarization conversion, linear-to-circular polarization conversion, broadband absorption, near-field imaging, two beam splitting, and four beam splitting. Compared with the existing reports, the structure pattern designed in this paper is completely composed of photosensitive silicon, which greatly reduces the complexity of the pattern and the difficulty of device manufacturing. At the same time, this paper makes use of the continuously adjustable conductivity of photosensitive silicon to generate a variety of coding states, making the function of the metasurface more abundant. Compared with the single-function metasurface, it has greater advantages in integration and other aspects. In a word, the metasurface proposed in this paper is more flexible in switching functions and can realize a wider range of functions. It has excellent application prospects in terahertz modulation, stealth technology, communication system, and so on.

Key words optics at surfaces; terahertz; photosensitive silicon; reconfigurable metasurface; multifunction